A Highly Soluble Iron-based Posolyte Species with High Redox Potential for Aqueous Redox Flow Batteries

Jinxu Gao[†,∇], Kyumin Lee[‡,∇], Kiana Amini[‡], Roy G. Gordon[*,†,‡], Theodore A. Betley[*,†], Michael J. Aziz[*,‡]

[∇]These authors contributed equally to this work.

[*]Corresponding authors:
gordon@chemistry.harvard.edu (Roy G. Gordon);
betley@chemistry.harvard.edu (Theodore A. Betley);
maziz@harvard.edu (Michael J. Aziz).

[†] Department of Chemistry and Chemical Biology, Harvard University, 12 Oxford Street, Cambridge, Massachusetts 02138, USA.

[‡] Harvard John A. Paulson School of Engineering and Applied Sciences, 29 Oxford Street, Cambridge, Massachusetts 02138, USA.

Abstract

We present a novel iron-based posolyte redox species for an aqueous redox flow battery, (Tetrakis(2-pyridylmethyl)ethylenediamine)iron(II) dichloride, which is obtained by a simple synthetic route, shows a high redox potential of 0.788 V vs. SHE, and exhibits exceptional aqueous solubility of 1.46 M. Paired with bis(3-trimethylammonio)propyl viologen tetrachloride at neutral pH, the battery demonstrates an open-circuit voltage of 1.19 V and delivers good cycling performance, with a capacity fade rate of 0.28% per day and coulombic efficiency of 99.3%. Post-mortem chemical and electrochemical analyses of the posolyte species suggest future routes for stabilization of the complex. Among all the iron complexes with a redox potential above 0.4 V vs. SHE, this compound exhibits the highest solubility. These results offer valuable insights that can be applied to the development of future posolyte species for sustainable energy storage solutions.

Keywords

Aqueous redox flow battery, energy storage, posolyte, redox-active electrolytes, metallorganics.

1. Introduction

Designed for large-scale energy storage, aqueous redox flow batteries (ARFBs) have drawn substantial attention due to their inherent safety and potential for mass production[1]. In the past few years, many redox-active inorganics[2], organics[2b, 3] and metalorganics[3c, 4] have been studied in ARFBs. Although great progress has been made with the low-potential active species, it has proven extremely challenging to develop organic and metalorganic species with a high redox

potential without compromising molecular lifetime[4c, 4d, 5]; thus, very few redox-active electrolytes for use in the posolyte (positive electrolyte) of an ARFB have been reported. The need for low-cost high-potential redox-active materials draws much attention to iron-based complexes. Additionally, the solubility of the organic or metalorganic posolyte species is almost invariably lower than that of the negolyte (negative electrolyte) species against which it is paired[3b-d, 4c, 5b, 5c, 6]. This causes the volumetric energy density of the system to be limited primarily by the posolyte solubility and further motivates the search for suitable posolyte species.

In recent years, there has been growing interest in investigating the potential of Fe coordination complexes in ARFB systems, especially in the context of near-neutral pH environments. Ruan *et al.* carried out an assessment of tris(bipyridyl)iron complex in a neutral pH ARFB, which delivered a high redox potential of 1.03 V vs. SHE and an open-circuit voltage of 1.4 V against a methyl viologen negolyte[5c]. But there are two major challenges with tris(bipyridyl)iron complexes — low aqueous solubility and high-capacity fade rate — hindering the practical application of this posolyte species. Xiang *et al.* reported an iron complex $Fe(Dcbpy)_2(CN)_2^{4-/3-}$ with a high redox potential of 0.86 V vs. SHE, demonstrating an excellent solubility (1.22 M) and a moderate capacity fade rate of 0.22% per day[4c, 7]. Nevertheless, the generation of poisonous gas during synthesis and the complexity of chemical synthetic route might prevent this molecule from achieving low-cost production. Our group reported a new high redox potential molecule, tris(2,2'-bipyridine-4,4'-diyldimethanol) iron dichloride ($Fe(Bhmbpy)_3$), demonstrating its remarkable performance over 35 days of cycling as a posolyte active species in an ARFB with a high redox potential of 0.985 V vs. SHE[4d], which is more than 0.5 V higher than that of the most commonly utilized metalorganic posolyte species, $Fe(CN)_6^{3-/4-}$. Compared to all previously reported organic and metalorganic compounds with a higher redox potential than that of $Fe(CN)_6^{3-/4-}$, $Fe(Bhmbpy)_3$ exhibits the lowest capacity fade rate, 0.07%/day. Nevertheless, the chemically reversible dimerization of oxidized $Fe(Bhmbpy)_3$ at higher concentration limits the usage of this posolyte species in ARFB system.

Here, we investigated an iron-based complex, (Tetrakis(2-pyridylmethyl)ethylenediamine)iron(II) dichloride ($Fe^{II}(TPEN)Cl_2$), synthesized using simple methods and exhibiting outstanding aqueous solubility of 1.46 M in water and a high redox potential of 0.788 V vs. SHE. The TPEN chelating ligand was chosen both for its desirable electrochemical properties as well as the ligand's ability to coordinatively saturate the iron's primary coordination sphere. The presence of the six neutral donor functionalities in TPEN will serve to anodically shift the redox potential for the $Fe^{III/II}$ couple, making the polycationic iron complex an ideal posolyte candidate. Additionally, much like common chelating agents (e.g., ethylenediaminetetraacetate[15]), a single ligand binding to all six available coordination sites on the metal ion can prevent deleterious reactions during cell cycling. Of primary concern would be the formation of aggregated ferric-oxo structures resulting from reaction of the oxidized $(TPEN)Fe^{III}$ with the highly basic media. This type of aggregation would decrease the electroactive material concentration in the cell, limiting its performance. The TPEN architecture can potentially slow this reaction down, preserving the integrity of the posolyte. When paired with bis(3-trimethylammonio)propyl viologen tetrachloride ($(BTMAP\text{-}Vi)Cl_4$) in the negolyte, the full cell demonstrates an open-circuit voltage of 1.19 V at near-neutral pH. Good performance was observed over 10 days of cycling, with a moderate temporal capacity fade rate of 0.28%/day at 0.6 M posolyte concentration. Informed by the results of post-mortem chemical and electrochemical analyses, we hypothesize that the substitution of TPEN ligands by chloride

ions, with their ability to coordinate to the iron center[8], results in the formation of a new metal complex and plays a significant role in the observed capacity loss during cell cycling and we suggest future routes for stabilization of the complex. This work thereby advances the prospects for high-performance RFBs at near-neutral pH.

2. Results and Discussion

The polypyridylamine hexadentate ligand, N,N,N′,N′-tetrakis(2-pyridylmethyl)ethylenediamine (TPEN), is a chelating agent with a high affinity for transition metal ions, such as zinc[9], copper[10], and nickel[11]. TPEN is widely used in research to investigate the roles of metal ions in various biological processes[9, 12]. Inspired by the high chelation capacity of TPEN, we synthesized an iron complex, $Fe^{II}(TPEN)Cl_2$, as the posolyte species, to investigate the potential application of this metal chelator in aqueous redox flow batteries (**Figure 1a**, see the **Supporting Information** for detailed synthesis). Our synthetic routes for $Fe^{II}(TPEN)Cl_2$ are straightforward and conducted under mild conditions, such as room temperature, atmospheric pressure, and aqueous solutions. The structure of $Fe^{II}(TPEN)Cl_2$ is further confirmed by single-crystal XRD analysis (**Figure 1b**). It is worth noting that the hexadentate ligand is composed of two aliphatic nitrogen atoms ($N_{aliphatic}$) in the ethylenediamine linkage and four aromatic nitrogen atoms ($N_{aromatic}$) in the pyridine rings. The Fe–$N_{aliphatic}$ bond lengths are approximately 2.00 Å, and Fe–$N_{aromatic}$ bond lengths are in the range of 1.97–2.00 Å. The crystallographic information (CCDC number 2251732) is summarized in **Table S1** and **Table S2**. In the context of the octahedral geometry of the Fe(II) TPEN complex, the presence of low-spin d^6 systems with a t_{2g}^6 configuration highlights its heightened thermodynamic stability and kinetic inertness[16]. This stability is primarily derived from the utilization of ligands with strong field chelating properties, such as en, terpy, bpy, and phen[17]. The electron-rich nitrogen donor sites of TPEN play a crucial role in stabilizing the Fe(II) oxidation state, contributing significantly to the overall stability of the resulting complex. On the other hand, the Fe(III) oxidation state encounters challenges in achieving similar stability due to the removal of an electron, leading to the formation of a less stable complex. Notably, the stability constants of both the TPEN-Fe^{3+} and Fe^{2+} iron complexes in solution are reported to be around 14.6[10], suggesting that the redox potential of this TPEN complex, approximately 0.77 V[18], is well-suited for serving as a promising posolyte species in an aqueous redox flow battery. The solubility of $Fe^{II}(TPEN)Cl_2$ is 1.46 M in DI water (**Figure 1c** and **Supporting Information**, p2). In comparison with other iron complex-based posolyte species, $Fe^{II}(TPEN)$ has the highest aqueous solubility of any metalorganic molecule with a redox potential > 0.4 V vs. SHE (**Figure 1c**).

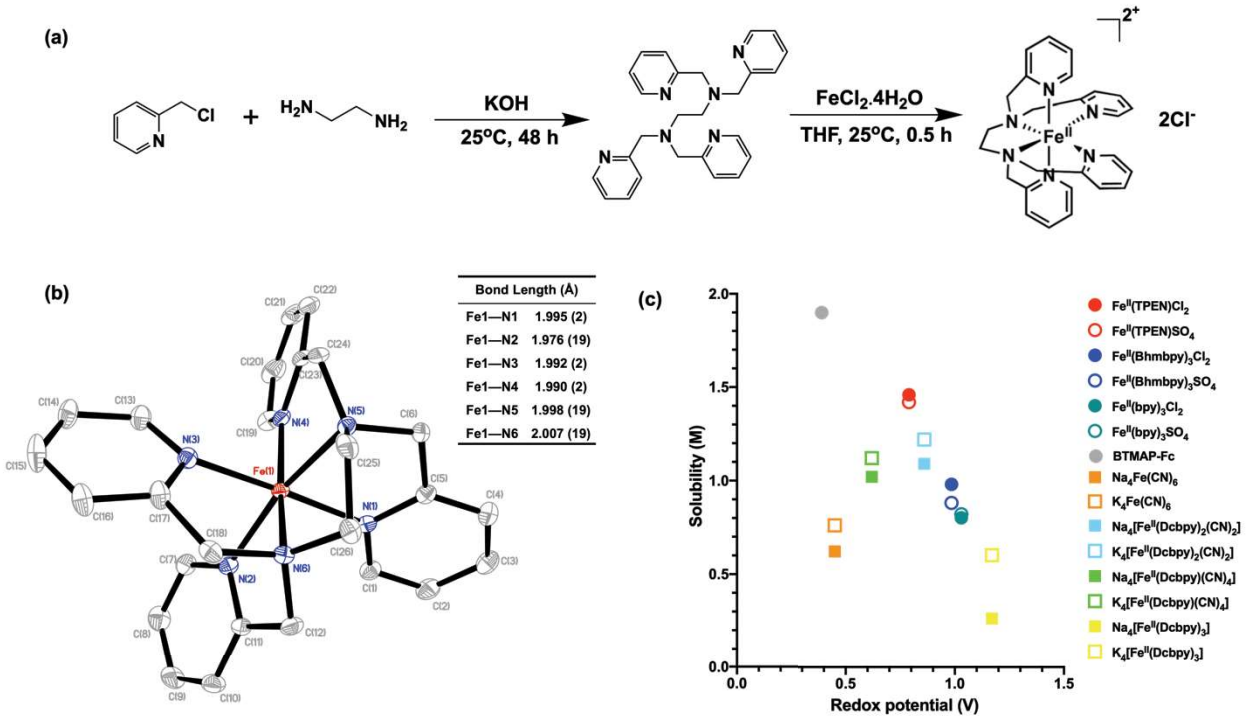


Figure 1. (a)
Synthetic route for $Fe^{II}(TPEN)Cl_2$. (b) Single-crystal X-ray diffraction (XRD) measurement for the structure with atom numbering scheme and selected geometric parameters (bond lengths with estimated standard deviations in parentheses). Displacement ellipsoids are drawn at the 50% probability level. (c) Comparison of solubility for iron complex-based posolyte species in deionized (DI) water[3c, 4b-d, 5c, 13]. Round dots represent iron complexes with anion counter ions (Cl^-, solid dots; SO_4^{2-}, hollow dots); square symbols represent iron complexes with cation counter ions (Na^+, solid square; K^+, hollow square).

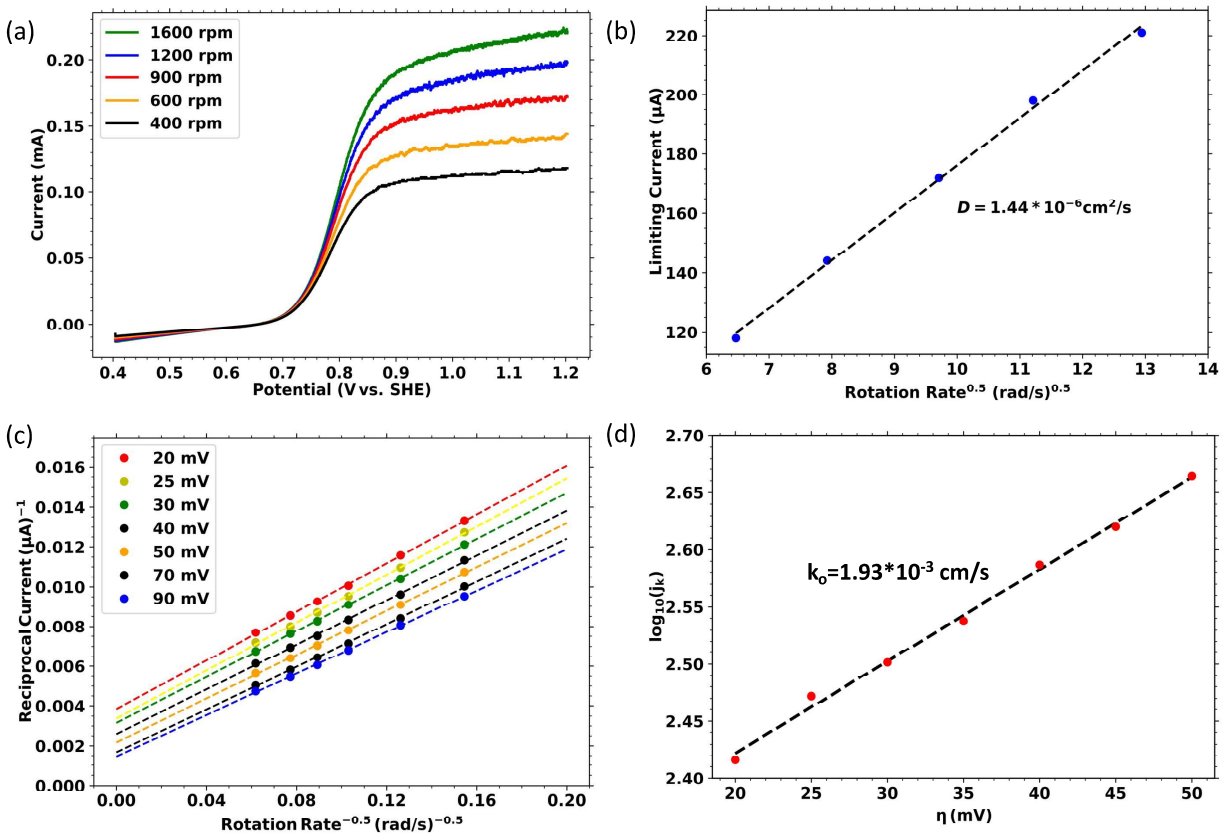


Figure 2. Rotating-disk-electrode experiment on 100 mM $Fe^{II}(TPEN)Cl_2$ in 1 M NaCl solution. (a) Linear sweep voltammograms on a glassy carbon rotating disk electrode at rotation rates between 400 and 2500 rpm with potential sweeping rate of 20 mV s^{-1}. (b) Levich plot of limiting current versus square root of rotation rate. Limiting current is taken as the current at 1.1 V in (a). (c) Koutecký–Levich plot (reciprocal current versus inverse square root of rotation rate) plot of 100 mM $Fe^{II}(TPEN)Cl_2$ in 1 M NaCl solution at different overpotentials. (d) Fitted Tafel plot of 100 mM $Fe^{II}(TPEN)Cl_2$ in 1 M NaCl solution.

The rotating disk electrode voltammetry method was used to measure the diffusion coefficient (D) of $Fe^{II}(TPEN)Cl_2$. The Levich equation was employed to calculate the diffusion coefficient by fitting the limiting current at various rotation rates, as shown in **Figure 2a**. The linear increase of the limiting current with the square root of the rotation rate depicted in **Figure 2b** suggests that the rate of the oxidation reaction is controlled by the transport of mass to the electrode surface. The diffusion coefficient of the reduced species was found to be 1.44×10^{-6} cm^2 s^{-1}, which is similar to the values reported for other iron complexes like $Fe(Bhmbpy)_3$[4d], $Fe^{II}(CN)_6$[4b], and $Fe^{II}(Dcbpy)_2(CN)_2$[4c]. The reciprocal kinetic current ($1/j_k$) was obtained from the Koutecký–Levich plot (**Figure 2c**) to determine the rate constant (k_0) for the charge transfer of $Fe^{II}(TPEN)Cl_2$ in the Tafel plot (**Figure 2d**) that was fitted. The rate constant for $Fe^{II}(TPEN)Cl_2$ is close to those of $Fe(Bhmbpy)_3$[4d], 9,10-anthraquinone-2,7-disulphonic acid (AQDS)[2b] and 2,6-dihydroxyanthraquinone (2,6-DHAQ)[3a].

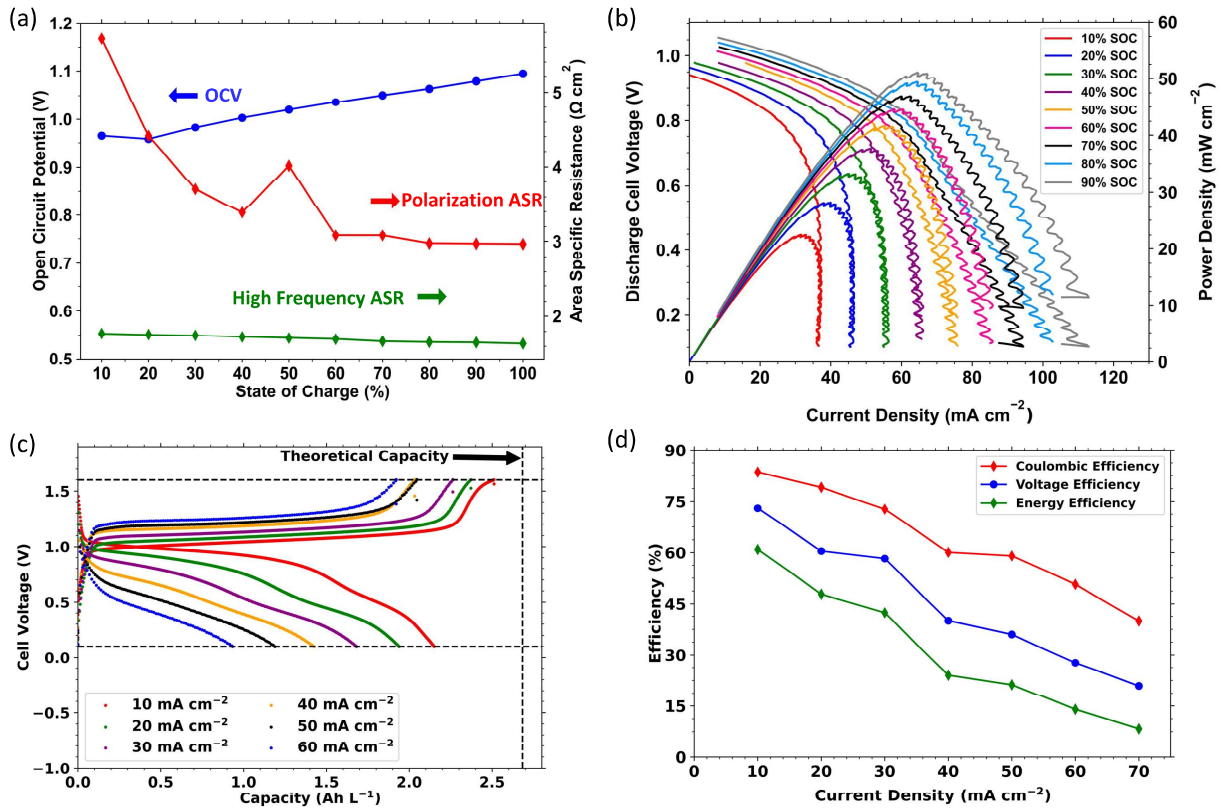


Figure 3. Power-density and Galvanostatic analysis. Performance of ARFB assembled with 0.1 M Fe(TPEN)Cl_2 in 1 M NaCl solution as the posolyte (6 mL) and (BTMAP-Vi)Cl_4 in 1 M NaCl solution as the negolyte (30 mL, 0.06 M oxidized (BTMAP-Vi)Cl_4, 0.01 M singly reduced (BTMAP-Vi)Cl_4 assembled with Selemion DSV-N as the anion exchange membrane. (a) OCV and high frequency and polarization ASR versus SOC for ARFB The cell cycling tests were conducted in a N_2-filled glove box. (b) Cell voltage and power density during discharge at various SOC. (c) Galvanostatic charge-discharge curves at various current densities (10, 20, 30, 40, 50, 60 and 70 mA cm^{-2}) with 1.6 V and 0.1 V cutoffs. The capacity is presented in units of ampere-hours per liter of posolyte. The theoretical capacity is indicated by the vertical dashed line. (d) Coulombic, voltage, and energy efficiency vs. applied current density.

Figure 3a displays an increase in the open circuit voltage (OCV) of the battery from 0.97 V at 10% state of charge (SOC) to 1.1 V at 100% SOC. The high-frequency area-specific resistance (ASR) of the battery is consistently slightly over 1.6 Ω cm^2 across all SOC ranges, with the membrane resistance being the primary contributor. The polarization resistance varies from 2.9 to 5.7 Ω cm^2, indicating that about 30–55% of the total resistance of the cell can be attributed to the membrane resistance. In **Figure 3b**, the polarization curves obtained at varying SOC levels show that the Fe(TPEN)Cl_2 battery reaches a peak power density of 51 mW/cm^2 at 90% SOC. The accessed capacity and round-trip efficiencies of the battery were evaluated through galvanostatic charging and discharging at various applied current densities, as shown in **Figure 3c** and **Figure 3d**. The results indicate that the accessible capacity of the battery decreases at higher current densities in the absence of voltage holds, owing to higher ohmic losses and mass transport overpotentials in the system. This leads to larger overpotentials and lower voltage efficiencies, as seen in **Figure 3d**.

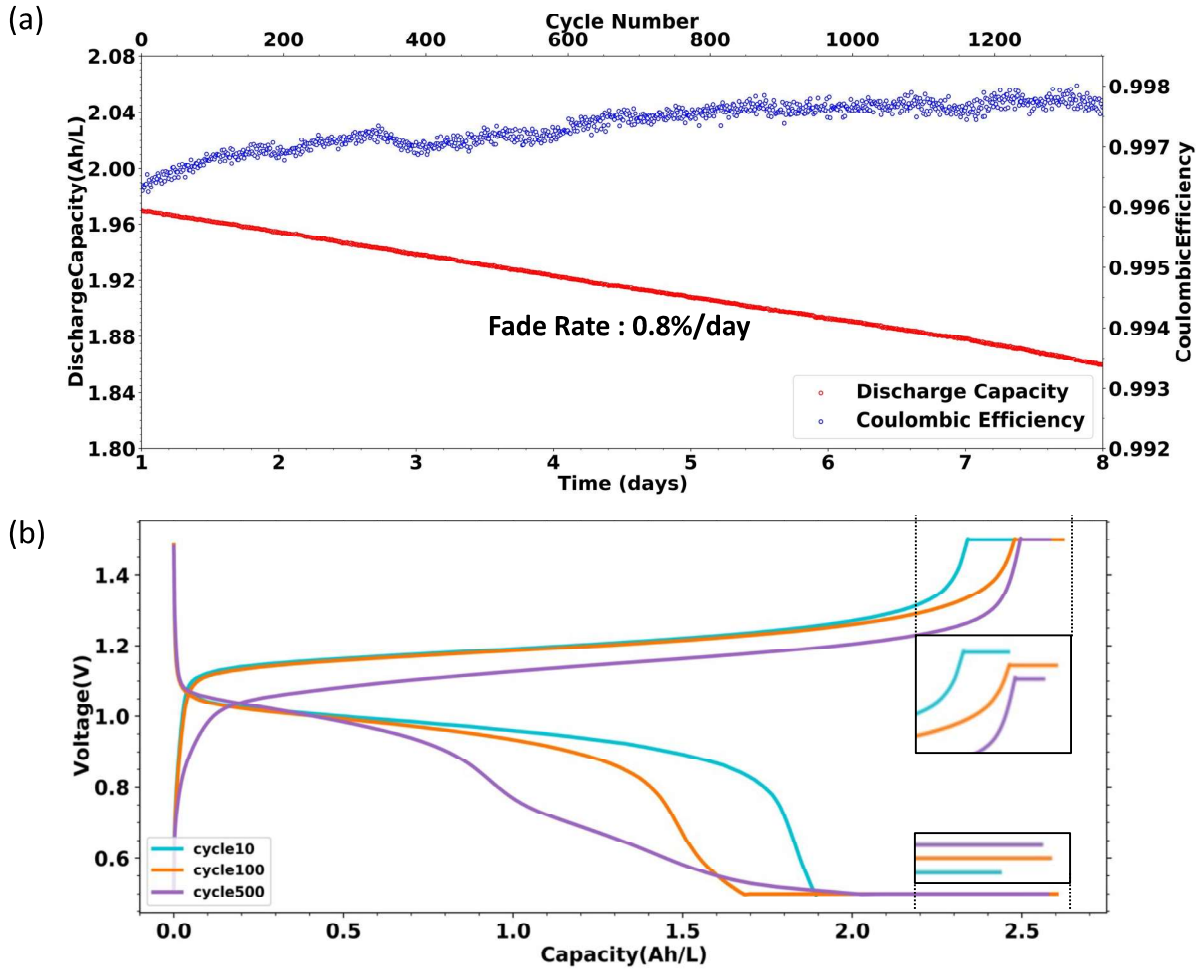


Figure 4. Cell cycling of a near-neutral ARFB assembled with 0.1 M Fe(TPEN)Cl_2 in 1 M NaCl solution as the posolyte (5 mL) and (BTMAP-Vi)Cl_4 in 1 M NaCl solution as the negolyte (30 mL, 0.06 M oxidized (BTMAP-Vi)Cl_4, 0.01 M singly reduced (BTMAP-Vi)Cl_4, with Selemion DSV-N as the anion exchange membrane. The cell cycling tests were conducted in a N_2-filled glove box. The capacity is presented in units of ampere-hours per liter of posolyte. (a) Charge and discharge capacities and coulombic efficiency versus time and cycle number operating with a constant current (30 mA cm^{-2}) followed by constant potentials of 1.5 V (charging) and 0.5 V (discharging). The dashed line shows the starting and the end date used for calculation of the capacity fade rate. (b) Charge-discharge voltage-capacity profiles of Fe(TPEN)Cl_2 from selected cycles in (a). The dashed line shows the theoretical capacity (2.68Ah/L). The traces are displaced vertically in the insets so as to identify the accessed capacity in each case.

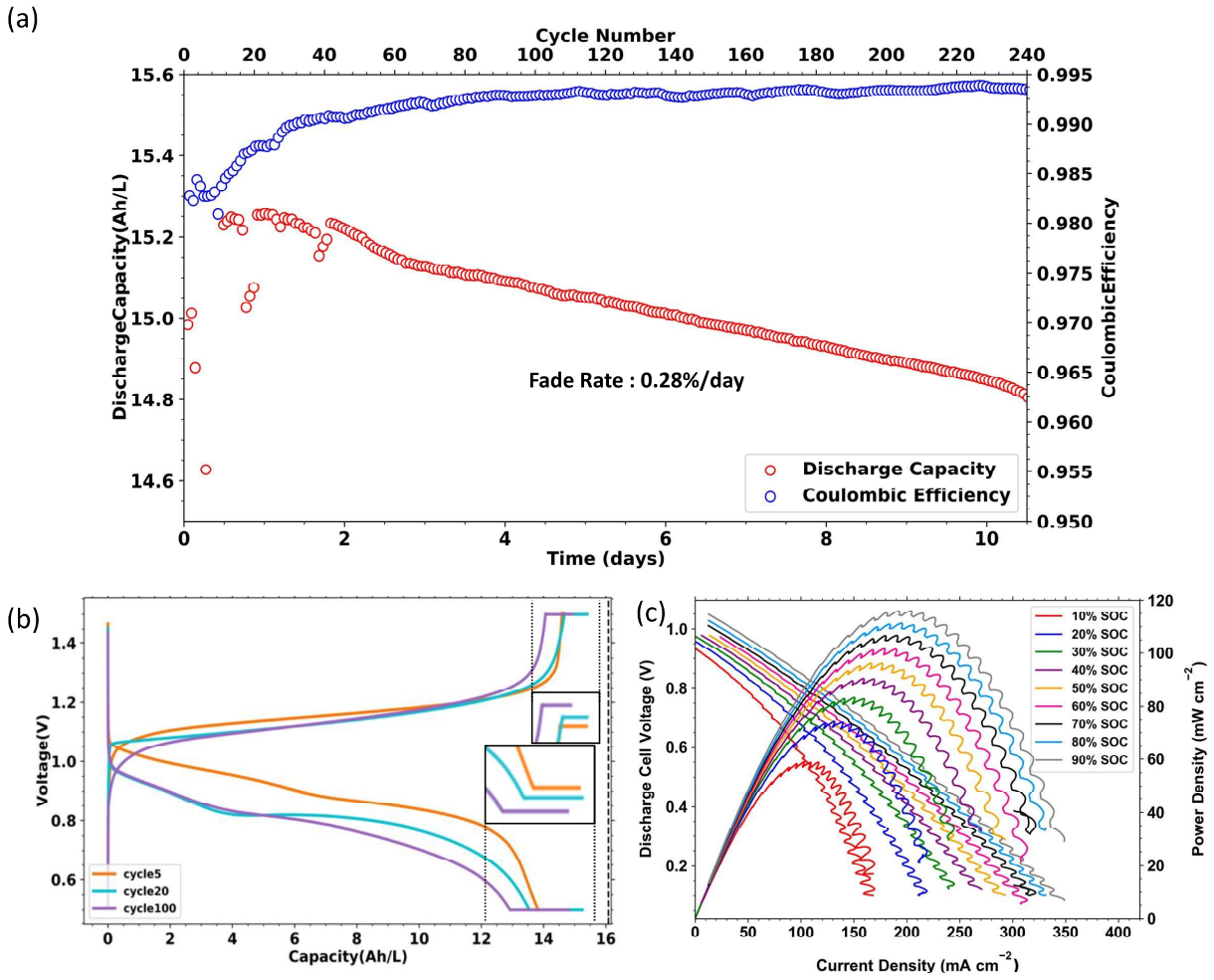


Figure 5. Cell cycling and power density analysis of a near-neutral ARFB using 0.6 M $Fe^{II}(TPEN)Cl_2$ in 4.8 mL of water as the posolyte and $(BTMAP\text{-}Vi)Cl_4$ in 1 M NaCl solution as the negolyte (30 mL, 0.7 M oxidized $(BTMAP\text{-}Vi)Cl_4$, 0.01 M singly reduced $(BTMAP\text{-}Vi)Cl_4$, with Selemion DSV-N as the anion exchange membrane. The cell cycling tests were conducted in a N_2-filled glove box, and the capacity is reported in ampere-hours per liter of posolyte. (a) Charge and discharge capacities and coulombic efficiency versus time and cycle number operating with a constant current (30 mA cm^{-2}) followed by constant potentials of 1.5 V (charging) and 0.5 V (discharging). The endpoints of the dashed line denote the interval used for evaluation of the capacity fade rate. (b) Charge-discharge voltage-capacity profiles of $Fe(TPEN)Cl_2$ from selected cycles in (a). Dashed line indicates the theoretical capacity (16.08 Ah/L). (c) Cell voltage and power density during discharge at various SOC.

To investigate the battery performance, $Fe(TPEN)Cl_2$ was first cycled in low concentration. A near-neutral pH ARFB was assembled using 0.1 M $Fe(TPEN)Cl_2$ in 5.5 mL of 1 M NaCl solution as the posolyte (0.0147Ah) and $(BTMAP\text{-}Vi)Cl_4$ in 1 M NaCl solution as the negolyte, separated by a Selemion DSV-N anion-exchange membrane, which delivered a working voltage of ~1.1 V. **Figure 4a** depicts the coulombic efficiency of the battery operated with a constant current of 30

mA cm^{-2} with constant potentials of 1.5 V (discharging) and 0.5 V (charging) during 8 days of operation. The battery capacity initially increased during the first day of operation, reaching a maximum capacity of 14.3 Ah, corresponding to 97% of the theoretical capacity. The small difference (less than 3%) between realized capacity and the theoretical value could come from errors in electrolyte volume measurement or the presence of redox-inactive impurities. During 8 days of full SOC range cycling, the temporal capacity fade rate of the battery was 0.8%/day. **Figure 4b** shows the charge-discharge voltage-capacity profiles of $Fe(TPEN)Cl_2$ from selected cycles. During the initial cycles, the cell exhibited a single plateau during discharge at approximately 1.0 V. However, as the number of cycles increased, the discharge voltage profile displayed a second plateau at a lower voltage of 0.7 V. This observation implies a plausible transformation of oxidized form of the posolyte species into two distinct redox-active species, with one of them possessing a lower reduction potential, whereas the negolyte species, $(BTMAP\text{-}Vi)Cl_4$, a well-characterized compound in the previous publication[3c], does not appear to be a contributing factor in this regard.

To investigate cycling performance at a higher concentration, we constructed a cell with ~5.0 mL of 0.6 M $Fe(TPEN)Cl_2$ in DI water (capacity-limiting side) paired with 30 mL of 0.46 M $(BTMAP\text{-}Vi)Cl_4$ in DI water operated under the same protocol described for the battery test at 0.1 M. In our system, the challenges posed by high viscosity at elevated concentrations led us to select an optimal concentration of 0.6M for high-concentration cell cycling. For future advancements in cell cycling at higher concentrations, operation at elevated temperature along with the development of a porous electrode architecture that can mitigate these challenges will be key enablers. After 10 days of full range cell cycling, a temporal fade rate of 0.28%/day was observed (**Figure 5a**). The voltage-capacity profiles of the battery from selected cycles are shown in **Figure 5b**, with a second plateau during discharge at around 0.7 V. Based on the cycling performance, $Fe(TPEN)Cl_2$ was compared with other previously reported organic and metalorganic positive electrolytes (posolytes) used as the capacity-limiting components in batteries. When compared to these previously reported redox-active organic and metalorganic compounds employed as aqueous posolyte species, $Fe(TPEN)Cl_2$ demonstrates a superior combination of cycling stability, high solubility, and a high redox potential, as illustrated in **Figure 6** and detailed in **Table S3**. This work highlights new avenues for increasing the energy density of aqueous organic/metalorganic flow batteries.

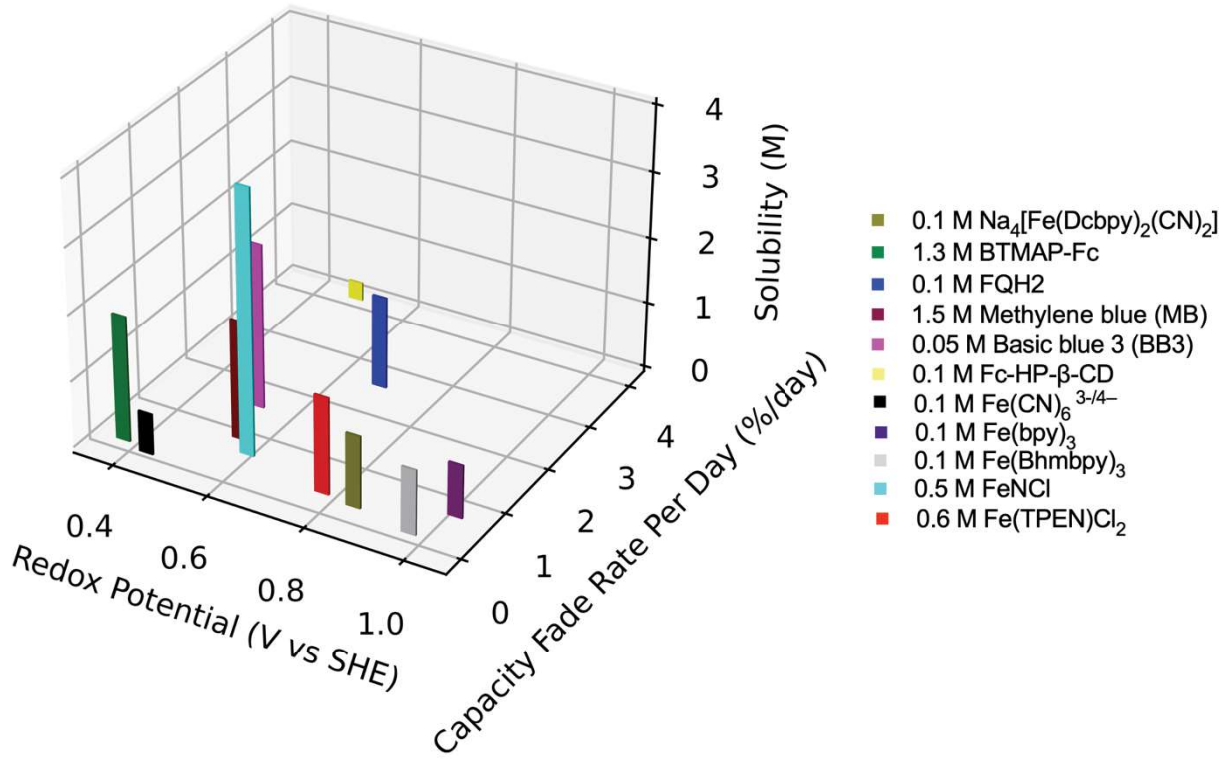


Figure 6. Comparison of present work with $Fe(TPEN)Cl_2$ and previously reported organic and metalorganic posolytes tested as the capacity limiting side of a battery. The numbers are taken from the refs [3c, 4c, 4d, 5c, 6d, 6e, 13a, 14]. Further information regarding these posolytes can be found in **Table S3**.

To further study the composition of the electrolytes before and after cycling, several post-mortem analysis techniques, including cyclic voltammetry, NMR and mass spectrometry were used. From polarization curves at varied SOC (**Figure 5c**), $Fe(TPEN)Cl_2$ delivers a peak power density of 116 mW cm^{-2} at 90% SOC and 96 mW cm^{-2} at 50% SOC. The ex-situ cyclic voltammetry (**Figure S6**) exhibits a new reduction peak at 0.25 V vs. SHE, indicating the production of new species in the posolyte during cycling. To investigate the possible structures of redox-active electrolytes generated during cell cycling, the cycled posolyte was analyzed by mass spectrometry. The raw mass spectrometry data and theoretical isotopic pattern are shown in **Figure S4**. Other than $[C_{26}H_{28}FeN_6]^{2+}$ (m/z=240.0853, **Fig S4a**) and $[C_{26}H_{28}FeN_6]^{3+}$ (m/z=160.0569, **Fig S4c**), the charged ions for $Fe(TPEN)Cl_2$ in reduced and oxidized forms, new charged ions were found in the post-cycling posolyte (**Figure S4b, S4d, S4e**). This might be associated with the formation of new complex species with chloride ions attached to the iron center (**Figure S5**). The ^{1}H-NMR analysis and cyclic voltammogram of posolytes, both before and after cycling, revealed the presence of new peaks when the cell was stopped in the fully charged state, suggesting the formation of new species during the cell cycling (**Figure S3, Figure S6**). To improve the performance of the battery, a comprehensive investigation of the decomposition mechanism of $Fe(TPEN)Cl_2$ is an important direction for future studies. In light of the hypothesized ligand substitution reaction by chloride ions, the impact of counter ions on the stability of $Fe(TPEN)Cl_2$ should be explored.

3. Conclusion

A simple synthetic route to the aqueous metalorganic redox-active posolyte species $Fe(TPEN)Cl_2$ was developed. The redox potential of 0.788 V vs. SHE of $Fe(TPEN)^{2+/3+}$ is fully one-third of a volt above that of $Fe(CN)_6^{3-/4-}$, which is the most commonly used posolyte species in aqueous organic or metalorganic flow batteries. $Fe^{II}(TPEN)Cl_2$ exhibits the highest solubility, 1.46 M, of all iron coordination complexes that exhibit a redox potential above 0.4 V vs. SHE. A flow cell comprising the chloride salts of a $Fe(TPEN)Cl_2$ posolyte (0.6 M) and a $(BTMAP\text{-}Vi)Cl_4$ negolyte (0.71 M) separated by a Selemion DSV-N anion-exchange membrane demonstrated an open-circuit voltage of 1.19 V at near-neutral pH and a capacity fade rate of 0.28%/day. The capacity fade appears to be caused by posolyte decomposition. Post-cycling analysis by mass spectrometry and CV leads us to hypothesize a mechanism of ligand substitution by chloride ions; this suggests potential routes for future research on stabilization of the complex. In comparison with previously reported redox-active organic and metalorganic compounds utilized as aqueous posolyte species, $Fe(TPEN)Cl_2$ exhibits a superior combination of cycling stability, high solubility, and high redox potential (**Figure 6**, **Table S3**). This work points out new development routes to increase the energy density of aqueous organic/metalorganic flow batteries.

4. Experimental Section

4.1 Materials and instrumentation

2-Picolyl chloride hydrochloride and ethylenediamine were purchased from Sigma Aldrich Inc. Other reagents were purchased from VWR International and utilized without further purification, unless specified otherwise. ^1H NMR and ^{13}C NMR spectra were measured on Varian INOVA 500 spectrometers operating at a frequency of 500 MHz. Electrospray ionization-mass spectrometry (ESI-MS) was conducted on a Bruker Impact HD q-TOF Mass Spectrometer.

4.2 Cyclic voltammetry

Cyclic voltammetry measurements were captured using an electrochemical analyzer manufactured by CH instruments (model: CHI 608E). The experimental setup featured a three-electrode configuration comprising a glassy carbon working electrode, a platinum counter electrode, and an Ag/AgCl reference electrode. Prior to and after each scan, the glassy carbon working electrode underwent polishing with an aluminum slurry.

4.3 Rotating disk electrode (RDE)

Rotating disk electrode (RDE) tests were performed using a Pine Instruments Modulated Speed Rotator AFMSRCE equipped with a 5 mm diameter glassy carbon working electrode (Pine Instruments E5PK), an Ag/AgCl reference electrode in 3 M NaCl solution (CHI), a graphite counter electrode and a Gamry Reference 3000 potentiostat.

4.4 Prolonged cell cycling

The long-term cycling performance of $Fe(TPEN)Cl_2$ was analyzed in a cell composed of ≈5.9 ml 0.1 M $Fe(TPEN)Cl_2$ in 1 M NaCl paired with 40 ml of 0.06 M $(BTMAP\text{-}Vi)Cl_4$ (oxidized)/0.01

M (BTMAP-Vi)Cl_4 (reduced) in 1 M NaCl. Excess capacity is used in the negolyte to ensure that the posolyte side is the capacity limiting side of the cell. The two half-cells were separated by a Selemion® DSV-N anion exchange membrane pretreated in 1 M NaCl solution. Three layers of carbon paper (SGL 39AA) baked at 400 ^oC overnight were used in each half-cell. The cell was cycled at a constant current of 30 mA cm^{-2}, followed by a constant charging voltage of 1.5 V and discharging voltage of 0.5 V until the current drops to 1 mA cm^{-2}.

Supporting Information

Supporting Information is available from the Wiley Online Library or from the author.

Acknowledgments

J.G. and K.L. contributed equally to this work. This research was supported by the National Science Foundation through grant CBET-1914543 and by U.S. DOE award DE-AC05-76RL01830 through PNNL subcontract 654799. K.A. was supported in part by the Natural Sciences and Engineering Research Council of Canada (NSERC) Postdoctoral Fellowship (PDF) program [application number PDF - 557232 – 2021]. The authors thank Dr. Shao-liang Zheng for single-crystal XRD analysis, and Jennifer Wang for mass spectrometry analysis. The authors also thank Dr. Yan Jing, Dawei Xi, Daniel Pollack, Dr. Emily Kerr, Eliza Spear, Abdulrahman Alfaraidi, Thomas George, Eric Fell, Jordan Sosa, Dr. Tatsuhiro Tsukamoto, Luana Cristina Italiano Faria, Michael Emanuel, Sofía Edgar, Taobo Wang, Prof. Matthew Suss, and Dr. Thomas Cochard for valuable discussions.

Conflict of Interest

R.G.G. and M.J.A. acknowledge significant financial stakes in Quino Energy, Inc., which might profit from the results reported here.

References

[1] a) O. Ellabban, H. Abu-Rub, F. Blaabjerg, *Renewable and Sustainable Energy Reviews* **2014**, *39*, 748-764; bJ. Rugolo, M. J. Aziz, *Energy & Environmental Science* **2012**, *5*.

[2] a) B. S. Jayathilake, E. J. Plichta, M. A. Hendrickson, S. R. Narayanan, *Journal of The Electrochemical Society* **2018**, *165*, A1630-A1638; b) B. Huskinson, M. P. Marshak, C. Suh, S. Er, M. R. Gerhardt, C. J. Galvin, X. Chen, A. Aspuru-Guzik, R. G. Gordon, M. J. Aziz, *Nature* **2014**, *505*, 195-198; c) Y. K. Zeng, T. S. Zhao, L. An, X. L. Zhou, L. Wei, *Journal of Power Sources* **2015**, *300*, 438-443; d) M. Ulaganathan, V. Aravindan, Q. Yan, S. Madhavi, M. Skyllas-Kazacos, T. M. Lim, *Advanced Materials Interfaces* **2016**, *3*.

[3] a) K. Lin, Q. Chen, M. R. Gerhardt, L. Tong, S. B. Kim, L. Eisenach, A. W. Valle, D. Hardee, R. G. Gordon, M. J. Aziz, M. P. Marshak, *Science* **2015**, *349*, 1529-1532; b) M.

Wu, M. Bahari, Y. Jing, K. Amini, E. M. Fell, T. Y. George, R. G. Gordon, M. J. Aziz, *Batteries & Supercaps* **2022**; c) E. S. Beh, D. De Porcellinis, R. L. Gracia, K. T. Xia, R. G. Gordon, M. J. Aziz, *ACS Energy Letters* **2017**, *2*, 639-644; d) S. Jin, Y. Jing, D. G. Kwabi, Y. Ji, L. Tong, D. De Porcellinis, M.-A. Goulet, D. A. Pollack, R. G. Gordon, M. J. Aziz, *ACS Energy Letters* **2019**, *4*, 1342-1348.

[4] a) K. L. Hawthorne, J. S. Wainright, R. F. Savinell, *Journal of The Electrochemical Society* **2014**, *161*, A1662-A1671; b) K. Gong, F. Xu, J. B. Grunewald, X. Ma, Y. Zhao, S. Gu, Y. Yan, *ACS Energy Letters* **2016**, *1*, 89-93; c) X. Li, P. Gao, Y.-Y. Lai, J. D. Bazak, A. Hollas, H.-Y. Lin, V. Murugesan, S. Zhang, C.-F. Cheng, W.-Y. Tung, Y.-T. Lai, R. Feng, J. Wang, C.-L. Wang, W. Wang, Y. Zhu, *Nature Energy* **2021**, *6*, 873-881; d) J. Gao, K. Amini, T. Y. George, Y. Jing, T. Tsukamoto, D. Xi, R. G. Gordon, M. J. Aziz, *Advanced Energy Materials* **2022**, *12,* 2202444.

[5] a) Y. Liu, M.-A. Goulet, L. Tong, Y. Liu, Y. Ji, L. Wu, R. G. Gordon, M. J. Aziz, Z. Yang, T. Xu, *Chem* **2019**, *5*, 1861-1870; b) T. Liu, X. Wei, Z. Nie, V. Sprenkle, W. Wang, *Advanced Energy Materials* **2016**, *6*:1501449; c) W. Ruan, J. Mao, S. Yang, Q. Chen, *Journal of The Electrochemical Society* **2020**, *167,* 070522.

[6] a) Y. Ji, M. A. Goulet, D. A. Pollack, D. G. Kwabi, S. Jin, D. Porcellinis, E. F. Kerr, R. G. Gordon, M. J. Aziz, *Advanced Energy Materials* **2019**, *9*; b) M. Wu, Y. Jing, A. A. Wong, E. M. Fell, S. Jin, Z. Tang, R. G. Gordon, M. J. Aziz, *Chem* **2020**, *6*, 1432-1442; c) Z. Zhao, B. Zhang, B. R. Schrage, C. J. Ziegler, A. Boika, *ACS Applied Energy Materials* **2020**, *3*, 10270-10277; d) Y. Li, Z. Xu, Y. Liu, S. Jin, E. M. Fell, B. Wang, R. G. Gordon, M. J. Aziz, Z. Yang, T. Xu, *ChemSusChem* **2021**, *14*, 745-752; e) B. Hu, C. DeBruler, Z. Rhodes, T. L. Liu, *J Am Chem Soc* **2017**, *139*, 1207-1214; f) C. DeBruler, B. Hu, J. Moss, X. Liu, J. Luo, Y. Sun, T. L. Liu, *Chem* **2017**, *3*, 961-978.

[7] D. G. Kwabi, Y. Ji, M. J. Aziz, *Chemical Reviews* **2020**, *120*, 6467-6489.

[8] D. T. Richens, *Chem. Rev.* **2005**, *105*, 42.

[9] C. E. R. Richardson, L. S. Cunden, V. L. Butty, E. M. Nolan, S. J. Lippard, M. D. Shoulders, *J Am Chem Soc* **2018**, *140*, 2413-2416.

[10] S. Schaefer-Ramadan, M. Barlog, J. Roach, M. Al-Hashimi, H. S. Bazzi, K. Machaca, *Bioorg Chem* **2019**, *87*, 366-372.

[11] L. E. Lieske, Arnold L. Rheingold, C. W. Machan, *Sustainable Energy & Fuels* **2018**, *2*, 1269-1277.

[12] a) Y. Guo, Y. Xu, Q. Bao, C. Shen, D. Ni, P. Hu, J. Shi, *ACS Nano* **2021**, *15*, 16286-16297; b) P. Vahidi Ferdowsi, R. Ng, J. Adulcikas, S. S. Sohal, S. Myers, *Molecules* **2020**, *25*.

[13] a) D. D. P. E.M. Fell, Y. Jing, V. Gutierrez-Venegas, R.G. Gordon, S. Granados-Focil, M.J. Aziz, **2022**; b) E. M. Fell, D. De Porcellinis, Y. Jing, V. Gutierrez-Venegas, T. Y. George, R. G. Gordon, S. Granados-Focil, M. J. Aziz, *Journal of The Electrochemical Society* **2023**, *170*.

[14] a) M. Park, E. S. Beh, E. M. Fell, Y. Jing, E. F. Kerr, D. Porcellinis, M. A. Goulet, J. Ryu, A. A. Wong, R. G. Gordon, J. Cho, M. J. Aziz, *Advanced Energy Materials* **2019**, *9*; b) C. Zhang, Z. Niu, S. Peng, Y. Ding, L. Zhang, X. Guo, Y. Zhao, G. Yu, *Adv Mater* **2019**, *31*, e1901052; c) H. Li, H. Fan, M. Ravivarma, B. Hu, Y. Feng, J. Song, *Chem Commun (Camb)* **2020**, *56*, 13824-13827.

[15] X. Yu, Y. Song, A. Tang, Tailoring manganese coordination environment for a highly reversible zinc-manganese flow battery, *J. Power Sources* **2021**, 507, 230295

[16] M. C. Carey, S. L. Adelman, J. K. McCusker, *Chem Sci* **2019**, *10*, 134-144.

[17] K. Atak, R. Golnak, J. Xiao, M. Pfluger, T. Brandenburg, B. Winter, E. F. Aziz, *Phys Chem Chem Phys* **2015**, *17*, 3409-3414.
[18] D. C. Harris, *Quantitative Chemical Analysis*, 7 ed., Macmillan, **2010**.

ADVANCED FUNCTIONAL MATERIALS

Supporting Information

for *Adv. Funct. Mater.*, DOI 10.1002/adfm.202310140

A Highly Soluble Iron-Based Posolyte Species with High Redox Potential for Aqueous Redox Flow Batteries

*Jinxu Gao, Kyumin Lee, Kiana Amini, Roy G. Gordon, Theodore A. Betley and Michael J. Aziz**

Supporting Information

A Neutral pH Aqueous Organic Flow Battery using a Novel Iron-based Complex as Redox Active Species for Posolyte

Jinxu Gao[†,∇], Kyumin Lee[‡,∇], Kiana Amini[‡], Roy G. Gordon[*,†,‡], Theodore A. Betley[*,†], Michael J. Aziz[*,‡]

[∇]These authors contributed equally to this work.

[*]Corresponding authors:
gordon@chemistry.harvard.edu (Roy G. Gordon);
betley@chemistry.harvard.edu (Theodore A. Betley);
maziz@harvard.edu (Michael J. Aziz).

[†] Department of Chemistry and Chemical Biology, Harvard University, 12 Oxford Street, Cambridge, Massachusetts 02138, USA.

[‡] Harvard John A. Paulson School of Engineering and Applied Sciences, 29 Oxford Street, Cambridge, Massachusetts 02138, USA.

Page numbers	Table of Contents
2	Materials and instrumentation
2	Single-crystal X-ray diffraction
2	Solubility tests
2	Cyclic voltammetry
2	Rotating disk electrode (RDE) tests
2	Polarization and galvanostatic tests
3	Prolonged cell cycling
3	ESI-MS measurement
4	Synthesis of N,N,N′,N′-tetrakis(2-pyridylmethyl)ethylenediamine (TPEN)
4	**Figure S1.** ^{1}H NMR spectrum of ligand TPEN in DMSO-d_6
5	Synthesis of [Fe(TPEN)]Cl_2
5	**Figure S2.** ^{1}H NMR spectrum of [Fe(TPEN)]Cl_2 in D_2O
6	**Table S1.** Crystallographic data and structure refinement for single crystal
7	**Table S2.** Geometric parameters (Å, º)
14	**Figure S3.** ^{1}H NMR spectra for posolyte before and after cycling
15	**Figure S4.** Raw mass spectrometry data for posolyte in BTMAP-Vi | Fe(TPEN) cell (0.6 M) after cycling
15	**Figure S5.** Proposed degradation mechanism of Fe(TPEN)Cl_2 during cell cycling.
16	**Figure S6.** Cyclic voltammograms of the negolytes and posolytes before and after cycling for ARFBs using Fe(TPEN)Cl_2 as the posolyte species.

16	**Figure S7.** Cyclic voltammograms of Fe(TPEN) and BTMAP-Vi.
17	**Table S3.** Comparison of $Fe(TPEN)Cl_2$ and other posolyte species reported previously.
17	References

Single-crystal X-ray diffraction

A crystal mounted on a diffractometer collected data at 100 K. The intensities of the reflections were collected by means of a Bruker APEX II CCD diffractometer (MoKα radiation, λ=0.71073 Å), and equipped with an Oxford Cryosystems nitrogen flow apparatus. The collection method involved 0.5° scans in ω at 28° in 2θ. Data integration down to 0.77 Å resolution was carried out using SAINT V8.37A[1] with reflection spot size optimization. Absorption corrections were made with the program SADABS. [1,2] The structure was solved by the Intrinsic Phasing methods and refined by least-squares methods again F^2 using SHELXT-2014[3] and SHELXL-2014[4] with OLEX 2 interface[5]. Non-hydrogen atoms were refined anisotropically, and hydrogen atoms were allowed to ride on the respective atoms. Crystal data as well as details of data collection and refinement are summarized in **Table S1**. Geometric parameters are shown in **Table S2**.

Solubility tests

The solubility limit of $Fe(TPEN)Cl_2$ in its reduced form was determined by gradually adding the salt of $Fe(TPEN)Cl_2$ into a specific volume of deionized (DI) water until no further solid could be dissolved. The concentration was then calculated based on the mass of $Fe(TPEN)Cl_2$ added into DI water and the final volume of the saturated solution. The resulting value for the solubility of the reduced form of $Fe(TPEN)Cl_2$ was found to be 1.46 M. We expect that the ferric form may exhibit even higher solubility due to its higher charge state, but direct measurements were impeded by the complexity of synthesizing and determining the oxidized form of $Fe(TPEN)Cl_3$.

Polarization and galvanostatic tests

Polarization and galvanostatic experiments were conducted for a cell compromised of ≈4.9 ml 0.1 M Fe(TPEN) in 1 M NaCl (47.2 C theoretical capacity) paired with 30 ml of 0.06 M BTMAP-Vi (oxidized)/0.01 M BTMAP-Vi (reduced) (173.7 C theoretical capacity) in 1 M NaCl. Excess capacity is used in the negolyte to ensure that the posolyte side is the capacity limiting side of the cell. The two half-cells were separated by a Selemion® DSV-N anion exchange membrane pretreated in 1 M NaCl solution. 3 layers of carbon paper (SGL 39AA) baked at 400°C overnight were used in each half-cell.

For polarization tests at different states of charges, the battery was first charged/discharged at 30 mA cm^{-2}. constant current followed by potential holds at 1.5 V (charge) and 0.5 V (discharge) until the current drops to 1 mA cm^{-2}. With this method the full accessed capacity of the cell is

determined. Consequently, the battery is charged to different states of charges (calculated from the percentage of the full accessed capacity) with 10% SOC intervals. At each SOC, the open-circuit voltage (OCV) of the battery is measured and the high-frequency area-specific resistance (ASR) are calculated from the Electrochemical Impedance Spectroscopy (EIS) measurements. Electrochemical impedance spectroscopy (EIS) was performed at SOCs between 10 and 100% at open-circuit potential with 10 mV perturbation and with frequency ranging from 1 to 100,000 Hz. Consequently, the potential is swept from 1.4 V to 0 V and the output current densities are measured for construction of the polarization curves. The polarization ASR is found from the slope of the linear region of the polarization curve between 1.3 V and 1.1 V.

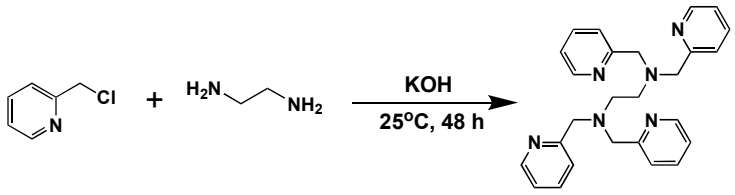
The galvanostatic tests were conducted at different applied current densities between 10 to 60 mA cm^{-2}. A constant current density is applied during both charge and discharge phases (with no potential holds) with 1.5 V and 0.5 V cut-off values. Consequently, the coulombic, voltage and energy efficiencies are calculated for each current density.

ESI-MS measurement

Samples are diluted with HPLC-grade water to 10 μM. High-resolution LC-MS analysis was performed in the Small Molecule Mass Spectrometry Facility at Harvard University on a MiniLIMS. The elution solution is 0.1% v/v formic acid in acetonitrile. The ESI mass spectra were recorded in positive ionization mode.

Synthesis

Synthesis of N,N,N′,N′-tetrakis(2-pyridylmethyl)ethylenediamine (TPEN)



The ligand was prepared by modification of a literature procedure[7]. 2-Picolyl chloride hydrochloride (13.65 g, 83.2 mmol) in 10 mL of water was neutralized by slow addition of 20 mL of a 4 M KOH solution. To this solution, 1.5 mL (18.2 mmol) of ethylenediamine was added dropwise. The reaction mixture was stirred at room temperature for 48 hours. During this time, the pH of the mixture was maintained between 8 and 10 by periodic dropwise addition of a 4 M solution of KOH. A white precipitate was then filtered and washed with 80 mL of water, and dried in vacuo for 24 h. Yield: 88.3 % (5.2 g, 12.2 mmol). The NMR spectra are shown in **Figure S1**.

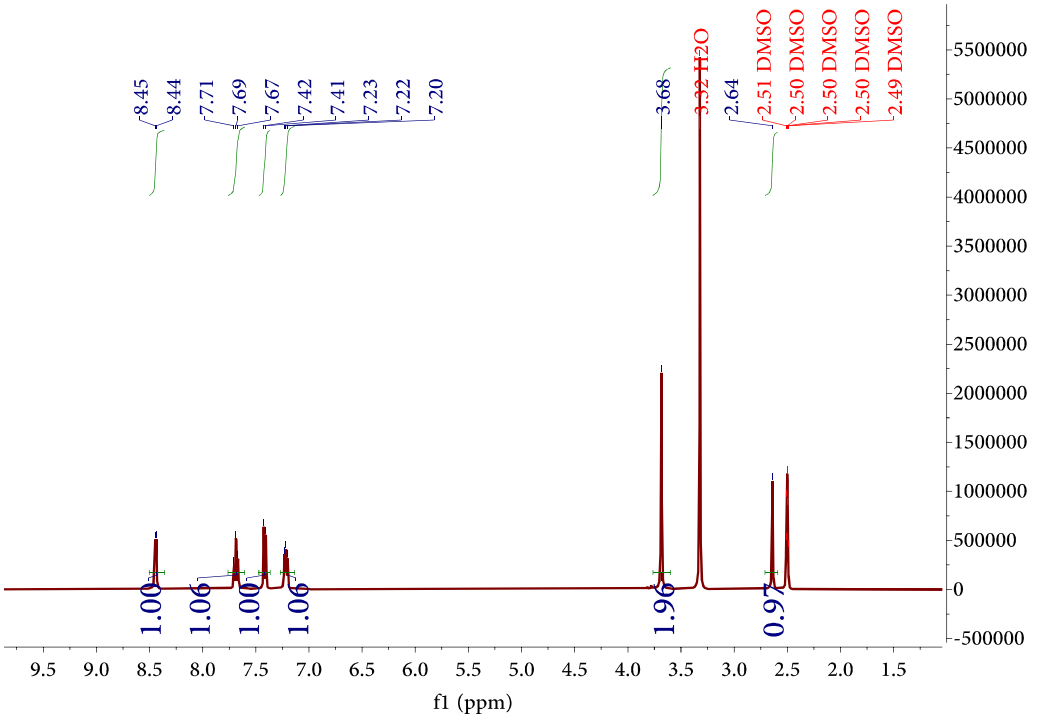
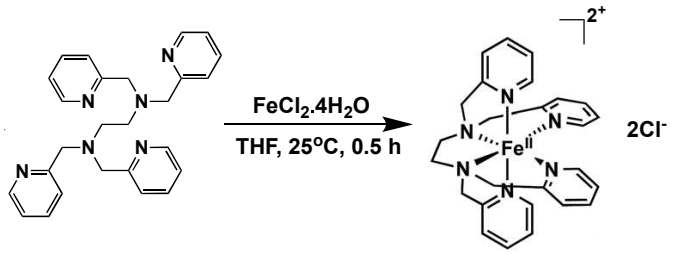


Figure S1. ^{1}H NMR spectrum of ligand TPEN in DMSO-d_6. ^{1}H NMR (400 MHz, DMSO-d_6) δ 8.45 (d, 4H), 9.13 7.69 (t, 4H), 7.42 (d, 4H), 7.22 (t, 4H), 3.68 (s, 8H), 2.64 (s, 4H).

Synthesis of [Fe(TPEN)]Cl_2



4.35 g of N, N, N′, N′-tetrakis(2-pyridylmethyl)ethylenediamine (10.2 mmol) was added to 200 mL anhydrous tetrahydrofuran under nitrogen gas. Then a solution of $FeCl_2 \cdot 4H_2O$ (2.03 g, 10.2 mmol) in anhydrous THF was added to the solution under vigorous stirring. After 30 minutes, ethyl acetate was added to the solution to collect the yellow solid. The crude product was washed with ethyl acetate, and the final yellow precipitate was obtained by filtration. Yield: 4.78 g (84.6 %).

MS (ESI) m/z for $(C_{26}H_{28}FeN_6)^{2+}$: calculated 240.0857, observed 240.0853.

The ^{1}H NMR spectrum of [Fe(TPEN)]Cl_2 is shown in **Figure S2**. The single-crystal XRD data are shown in **Table S1** and **Table S2**.

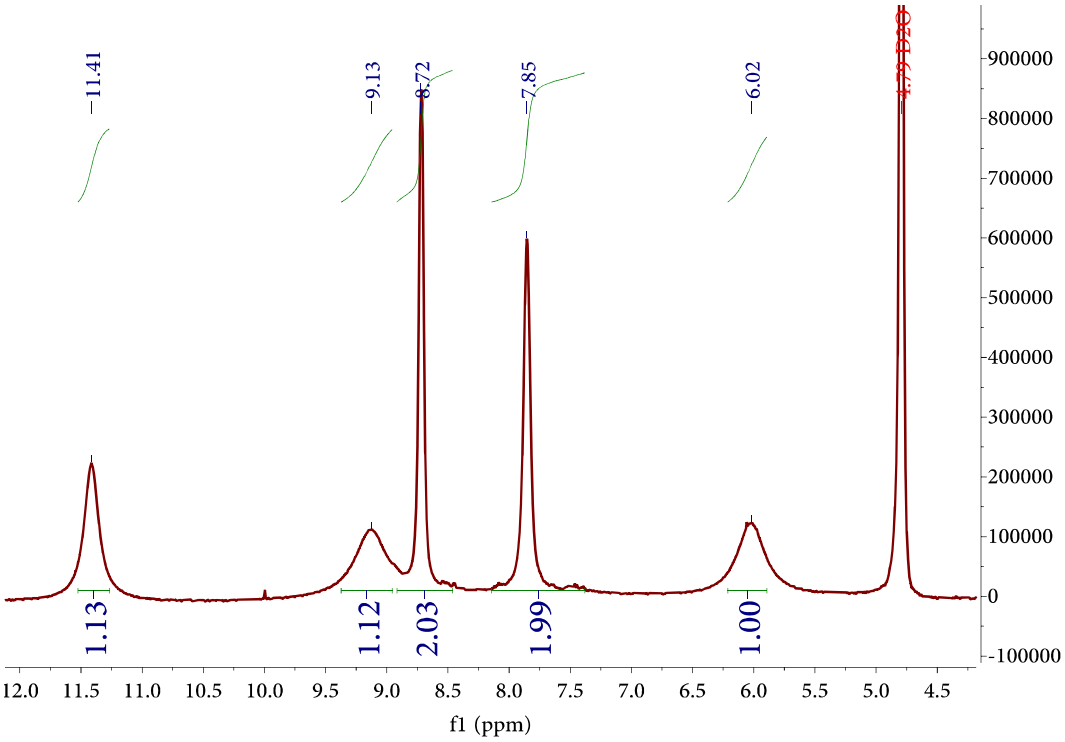


Figure S2. ^{1}H NMR spectrum of [Fe(TPEN)]Cl_2 in D_2O. ^{1}H NMR (400 MHz, D_2O) δ 11.41 (s, 4H), 9.13 (s, 4H), 8.72 (s, 8H), 7.85 (s, 8H), 6.02 (s, 4H).

Table S1. Crystallographic data and structure refinement for single crystal

Crystal data for $[Fe(TPEN)](ClO_4)_2 \cdot 1.33H_2O$	
Chemical formula	$C_{28}H_{32.67}Cl_2FeN_6O_{9.33}$
M_r	729.34
Crystal system, space group	Monoclinic, $P2_1/n$
Temperature (K)	100
a, b, c (Å)	13.8056 (17), 16.5420 (15), 14.0325 (12)
β (°)	102.985 (4)
V (Å^3)	3122.7 (5)
Z	4
Radiation type	Mo $K\alpha$
μ (mm^{-1})	0.72
Crystal size (mm)	0.18 × 0.03 × 0.02
Data collection	
Diffractometer	Bruker D8 goniometer with CCD area detector
Absorption correction	Multi-scan *SADABS*
T_{min}, T_{max}	0.753, 0.801
No. of measured, independent and observed [$I > 2\sigma(I)$] reflections	48835, 7124, 5243
R_{int}	0.065
$(\sin \theta/\lambda)_{max}$ (Å^{-1})	0.649
Refinement	
$R[F^2 > 2\sigma(F^2)]$, $wR(F^2)$, S	0.042, 0.101, 1.02
No. of reflections	7124
No. of parameters	476
No. of restraints	117
H-atom treatment	H-atom parameters constrained
$\Delta\rho_{max}$, $\Delta\rho_{min}$ (e Å^{-3})	0.62, -0.41

Computer programs: *SAINT* 8.37A (Bruker-AXS, 2015), *SHELXT2014* (Sheldrick, 2015), *SHELXL2014* (Sheldrick, 2015), Bruker *SHELXTL* (Sheldrick, 2015).

Table S2. Geometric parameters (Å, º)

Fe1—N2	1.9762 (19)	C13A—H13A	0.9500
Fe1—N4	1.990 (2)	C14A—C15A	1.396 (7)
Fe1—N3A	1.992 (2)	C14A—H14A	0.9500
Fe1—N3	1.992 (2)	C15A—C16A	1.382 (7)
Fe1—N1	1.995 (2)	C15A—H15A	0.9500
Fe1—N5	1.9985 (19)	C16A—C17A	1.408 (7)
Fe1—N6	2.0073 (19)	C16A—H16A	0.9500
N1—C5	1.350 (3)	C17A—C18	1.494 (3)
N1—C1	1.356 (3)	C18—H18C	0.9900
N2—C7	1.347 (3)	C18—H18D	0.9900
N2—C11	1.363 (3)	C18—H18A	0.9900
N4—C19	1.345 (3)	C18—H18B	0.9900
N4—C23	1.371 (3)	C19—C20	1.381 (3)
N5—C24	1.487 (3)	C19—H19	0.9500
N5—C25	1.495 (3)	C20—C21	1.383 (4)
N5—C6	1.502 (3)	C20—H20	0.9500
N6—C12	1.484 (3)	C21—C22	1.389 (4)
N6—C26	1.496 (3)	C21—H21	0.9500
N6—C18	1.502 (3)	C22—C23	1.381 (3)
C1—C2	1.377 (3)	C22—H22	0.9500
C1—H1	0.9500	C23—C24	1.506 (3)
C2—C3	1.386 (4)	C24—H24A	0.9900
C2—H2	0.9500	C24—H24B	0.9900
C3—C4	1.379 (4)	C25—C26	1.516 (3)
C3—H3	0.9500	C25—H25A	0.9900
C4—C5	1.390 (3)	C25—H25B	0.9900
C4—H4	0.9500	C26—H26A	0.9900
C5—C6	1.496 (3)	C26—H26B	0.9900

C6—H6A	0.9900	Cl1—O4	1.4333 (19)
C6—H6B	0.9900	Cl1—O1	1.4403 (17)
C7—C8	1.386 (3)	Cl1—O3	1.4411 (18)
C7—H7	0.9500	Cl1—O2	1.4436 (19)
C8—C9	1.381 (4)	Cl2—O6A	1.422 (15)
C8—H8	0.9500	Cl2—O8	1.422 (2)
C9—C10	1.391 (4)	Cl2—O7	1.431 (2)
C9—H9	0.9500	Cl2—O6	1.432 (2)
C10—C11	1.381 (3)	Cl2—O8A	1.434 (16)
C10—H10	0.9500	Cl2—O5	1.4427 (18)
C11—C12	1.506 (3)	Cl2—O7A	1.470 (15)
C12—H12A	0.9900	C1S—C2S	1.449 (10)
C12—H12B	0.9900	C1S—H1SA	0.9800
N3—C17	1.345 (3)	C1S—H1SB	0.9800
N3—C13	1.363 (12)	C1S—H1SC	0.9800
C13—C14	1.382 (12)	O1S—C2S	1.461 (9)
C13—H13	0.9500	O1S—C3S	1.50 (2)
C14—C15	1.390 (12)	C2S—O2S	1.191 (8)
C14—H14	0.9500	C3S—C4S	1.486 (10)
C15—C16	1.368 (12)	C3S—H3SA	0.9900
C15—H15	0.9500	C3S—H3SB	0.9900
C16—C17	1.389 (11)	C4S—H4SA	0.9800
C16—H16	0.9500	C4S—H4SB	0.9800
C17—C18	1.494 (3)	C4S—H4SC	0.9800
N3A—C17A	1.345 (3)	O1W—H1WA	0.8700
N3A—C13A	1.356 (7)	O1W—H1WB	0.8700
C13A—C14A	1.382 (8)		
N2—Fe1—N4	110.12 (8)	C13A—N3A—Fe1	126.1 (5)
N2—Fe1—N3A	86.44 (8)	N3A—C13A—C14A	123.3 (8)
N4—Fe1—N3A	91.75 (8)	N3A—C13A—H13A	118.3
N2—Fe1—N3	86.44 (8)	C14A—C13A—H13A	118.3
N4—Fe1—N3	91.75 (8)	C13A—C14A—C15A	118.6 (7)
N2—Fe1—N1	91.37 (8)	C13A—C14A—H14A	120.7

N4—Fe1—N1	89.08 (8)	C15A—C14A—H14A	120.7
N3A—Fe1—N1	177.81 (8)	C16A—C15A—C14A	118.3 (6)
N3—Fe1—N1	177.81 (8)	C16A—C15A—H15A	120.9
N2—Fe1—N5	166.98 (8)	C14A—C15A—H15A	120.9
N4—Fe1—N5	81.99 (8)	C15A—C16A—C17A	120.3 (6)
N3A—Fe1—N5	98.27 (8)	C15A—C16A—H16A	119.8
N3—Fe1—N5	98.27 (8)	C17A—C16A—H16A	119.8
N1—Fe1—N5	83.86 (8)	N3A—C17A—C16A	120.8 (4)
N2—Fe1—N6	81.55 (8)	N3A—C17A—C18	117.0 (2)
N4—Fe1—N6	167.39 (8)	C16A—C17A—C18	122.0 (4)
N3A—Fe1—N6	84.04 (8)	C17A—C18—N6	112.11 (19)
N3—Fe1—N6	84.04 (8)	C17—C18—N6	112.11 (19)
N1—Fe1—N6	95.57 (8)	C17—C18—H18C	109.2
N5—Fe1—N6	86.84 (8)	N6—C18—H18C	109.2
C5—N1—C1	116.8 (2)	C17—C18—H18D	109.2
C5—N1—Fe1	115.59 (15)	N6—C18—H18D	109.2
C1—N1—Fe1	127.58 (16)	H18C—C18—H18D	107.9
C7—N2—C11	117.8 (2)	C17A—C18—H18A	109.2
C7—N2—Fe1	129.63 (16)	N6—C18—H18A	109.2
C11—N2—Fe1	112.52 (15)	C17A—C18—H18B	109.2
C19—N4—C23	117.7 (2)	N6—C18—H18B	109.2
C19—N4—Fe1	130.38 (17)	H18A—C18—H18B	107.9
C23—N4—Fe1	111.91 (16)	N4—C19—C20	123.2 (2)
C24—N5—C25	114.39 (18)	N4—C19—H19	118.4
C24—N5—C6	109.71 (18)	C20—C19—H19	118.4
C25—N5—C6	110.07 (18)	C19—C20—C21	118.8 (3)
C24—N5—Fe1	105.29 (14)	C19—C20—H20	120.6
C25—N5—Fe1	106.02 (14)	C21—C20—H20	120.6
C6—N5—Fe1	111.22 (14)	C20—C21—C22	119.1 (2)
C12—N6—C26	114.51 (18)	C20—C21—H21	120.5
C12—N6—C18	109.55 (18)	C22—C21—H21	120.5
C26—N6—C18	110.09 (18)	C23—C22—C21	119.4 (2)
C12—N6—Fe1	105.19 (14)	C23—C22—H22	120.3
C26—N6—Fe1	106.15 (14)	C21—C22—H22	120.3

C18—N6—Fe1	111.23 (14)	N4—C23—C22	121.8 (2)
N1—C1—C2	123.4 (2)	N4—C23—C24	114.8 (2)
N1—C1—H1	118.3	C22—C23—C24	123.3 (2)
C2—C1—H1	118.3	N5—C24—C23	106.50 (18)
C1—C2—C3	119.0 (2)	N5—C24—H24A	110.4
C1—C2—H2	120.5	C23—C24—H24A	110.4
C3—C2—H2	120.5	N5—C24—H24B	110.4
C4—C3—C2	118.5 (2)	C23—C24—H24B	110.4
C4—C3—H3	120.7	H24A—C24—H24B	108.6
C2—C3—H3	120.7	N5—C25—C26	107.03 (18)
C3—C4—C5	119.5 (2)	N5—C25—H25A	110.3
C3—C4—H4	120.3	C26—C25—H25A	110.3
C5—C4—H4	120.3	N5—C25—H25B	110.3
N1—C5—C4	122.6 (2)	C26—C25—H25B	110.3
N1—C5—C6	115.8 (2)	H25A—C25—H25B	108.6
C4—C5—C6	121.5 (2)	N6—C26—C25	106.56 (19)
C5—C6—N5	112.00 (19)	N6—C26—H26A	110.4
C5—C6—H6A	109.2	C25—C26—H26A	110.4
N5—C6—H6A	109.2	N6—C26—H26B	110.4
C5—C6—H6B	109.2	C25—C26—H26B	110.4
N5—C6—H6B	109.2	H26A—C26—H26B	108.6
H6A—C6—H6B	107.9	O4—Cl1—O1	110.32 (12)
N2—C7—C8	122.7 (2)	O4—Cl1—O3	109.53 (13)
N2—C7—H7	118.7	O1—Cl1—O3	109.01 (11)
C8—C7—H7	118.7	O4—Cl1—O2	109.80 (13)
C9—C8—C7	119.1 (2)	O1—Cl1—O2	110.16 (11)
C9—C8—H8	120.4	O3—Cl1—O2	107.98 (11)
C7—C8—H8	120.4	O8—Cl2—O7	109.68 (17)
C8—C9—C10	118.8 (2)	O8—Cl2—O6	110.85 (18)
C8—C9—H9	120.6	O7—Cl2—O6	108.95 (17)
C10—C9—H9	120.6	O6A—Cl2—O8A	107.1 (14)
C11—C10—C9	119.4 (2)	O6A—Cl2—O5	121.4 (10)
C11—C10—H10	120.3	O8—Cl2—O5	110.02 (13)
C9—C10—H10	120.3	O7—Cl2—O5	108.30 (13)

N2—C11—C10	122.0 (2)	O6—Cl2—O5	108.98 (13)
N2—C11—C12	114.8 (2)	O8A—Cl2—O5	105.7 (9)
C10—C11—C12	123.1 (2)	O6A—Cl2—O7A	103.4 (14)
N6—C12—C11	107.02 (18)	O8A—Cl2—O7A	102.8 (14)
N6—C12—H12A	110.3	O5—Cl2—O7A	114.7 (8)
C11—C12—H12A	110.3	C2S—C1S—H1SA	109.5
N6—C12—H12B	110.3	C2S—C1S—H1SB	109.5
C11—C12—H12B	110.3	H1SA—C1S—H1SB	109.5
H12A—C12—H12B	108.6	C2S—C1S—H1SC	109.5
C17—N3—C13	115.5 (8)	H1SA—C1S—H1SC	109.5
C17—N3—Fe1	114.95 (16)	H1SB—C1S—H1SC	109.5
C13—N3—Fe1	127.3 (8)	C2S—O1S—C3S	119.3 (11)
N3—C13—C14	122.6 (14)	O2S—C2S—C1S	131.0 (8)
N3—C13—H13	118.7	O2S—C2S—O1S	121.9 (7)
C14—C13—H13	118.7	C1S—C2S—O1S	107.1 (6)
C13—C14—C15	119.6 (13)	C4S—C3S—O1S	112.9 (9)
C13—C14—H14	120.2	C4S—C3S—H3SA	109.0
C15—C14—H14	120.2	O1S—C3S—H3SA	109.0
C16—C15—C14	119.0 (12)	C4S—C3S—H3SB	109.0
C16—C15—H15	120.5	O1S—C3S—H3SB	109.0
C14—C15—H15	120.5	H3SA—C3S—H3SB	107.8
C15—C16—C17	117.5 (11)	C3S—C4S—H4SA	109.5
C15—C16—H16	121.3	C3S—C4S—H4SB	109.5
C17—C16—H16	121.3	H4SA—C4S—H4SB	109.5
N3—C17—C16	125.0 (7)	C3S—C4S—H4SC	109.5
N3—C17—C18	117.0 (2)	H4SA—C4S—H4SC	109.5
C16—C17—C18	116.3 (7)	H4SB—C4S—H4SC	109.5
C17A—N3A—C13A	118.4 (5)	H1WA—O1W—H1WB	109.5
C17A—N3A—Fe1	114.95 (16)		
C5—N1—C1—C2	2.4 (3)	N3A—C13A—C14A—C15A	0.4 (9)
Fe1—N1—C1—C2	-178.26 (19)	C13A—C14A—C15A—C16A	1.2 (8)

N1—C1—C2—C3	0.5 (4)	C14A—C15A—C16A—C17A	-4.5 (8)
C1—C2—C3—C4	-2.0 (4)	C13A—N3A—C17A—C16A	-5.0 (7)
C2—C3—C4—C5	0.5 (4)	Fe1—N3A—C17A—C16A	-177.4 (5)
C1—N1—C5—C4	-4.0 (3)	C13A—N3A—C17A—C18	-179.6 (5)
Fe1—N1—C5—C4	176.59 (18)	Fe1—N3A—C17A—C18	8.0 (3)
C1—N1—C5—C6	172.9 (2)	C15A—C16A—C17A—N3A	6.6 (7)
Fe1—N1—C5—C6	-6.5 (3)	C15A—C16A—C17A—C18	-179.0 (4)
C3—C4—C5—N1	2.6 (4)	N3A—C17A—C18—N6	-2.8 (3)
C3—C4—C5—C6	-174.1 (2)	C16A—C17A—C18—N6	-177.4 (5)
N1—C5—C6—N5	13.0 (3)	N3—C17—C18—N6	-2.8 (3)
C4—C5—C6—N5	-170.0 (2)	C16—C17—C18—N6	163.0 (7)
C24—N5—C6—C5	-129.3 (2)	C12—N6—C18—C17A	-119.4 (2)
C25—N5—C6—C5	104.0 (2)	C26—N6—C18—C17A	113.8 (2)
Fe1—N5—C6—C5	-13.2 (2)	Fe1—N6—C18—C17A	-3.6 (2)
C11—N2—C7—C8	-4.1 (4)	C12—N6—C18—C17	-119.4 (2)
Fe1—N2—C7—C8	176.40 (19)	C26—N6—C18—C17	113.8 (2)
N2—C7—C8—C9	1.1 (4)	Fe1—N6—C18—C17	-3.6 (2)
C7—C8—C9—C10	2.4 (4)	C23—N4—C19—C20	-0.8 (4)
C8—C9—C10—C11	-2.8 (4)	Fe1—N4—C19—C20	-178.11 (19)
C7—N2—C11—C10	3.7 (3)	N4—C19—C20—C21	2.0 (4)
Fe1—N2—C11—C10	-176.70 (19)	C19—C20—C21—C22	-1.5 (4)
C7—N2—C11—C12	-177.0 (2)	C20—C21—C22—C23	-0.2 (4)
Fe1—N2—C11—C12	2.6 (3)	C19—N4—C23—C22	-1.0 (3)
C9—C10—C11—N2	-0.3 (4)	Fe1—N4—C23—C22	176.82 (19)
C9—C10—C11—C12	-179.6 (2)	C19—N4—C23—C24	-179.7 (2)
C26—N6—C12—C11	-160.24 (19)	Fe1—N4—C23—C24	-1.9 (2)
C18—N6—C12—C11	75.5 (2)	C21—C22—C23—N4	1.4 (4)

Fe1—N6—C12—C11	-44.1 (2)	C21—C22—C23—C24	-179.9 (2)
N2—C11—C12—N6	28.3 (3)	C25—N5—C24—C23	-161.71 (19)
C10—C11—C12—N6	-152.4 (2)	C6—N5—C24—C23	74.1 (2)
C17—N3—C13—C14	-2.6 (13)	Fe1—N5—C24—C23	-45.7 (2)
Fe1—N3—C13—C14	159.7 (8)	N4—C23—C24—N5	32.1 (3)
N3—C13—C14—C15	0.5 (15)	C22—C23—C24—N5	-146.6 (2)
C13—C14—C15—C16	-3.4 (17)	C24—N5—C25—C26	158.81 (19)
C14—C15—C16—C17	8.2 (17)	C6—N5—C25—C26	-77.1 (2)
C13—N3—C17—C16	8.1 (11)	Fe1—N5—C25—C26	43.2 (2)
Fe1—N3—C17—C16	-156.5 (8)	C12—N6—C26—C25	158.04 (19)
C13—N3—C17—C18	172.5 (8)	C18—N6—C26—C25	-78.0 (2)
Fe1—N3—C17—C18	8.0 (3)	Fe1—N6—C26—C25	42.5 (2)
C15—C16—C17—N3	-11.1 (14)	N5—C25—C26—N6	-57.8 (2)
C15—C16—C17—C18	-175.7 (9)	C3S—O1S—C2S—O2S	6.1 (16)
C17A—N3A—C13A—C14A	1.5 (9)	C3S—O1S—C2S—C1S	-174.0 (14)
Fe1—N3A—C13A—C14A	173.0 (5)	C2S—O1S—C3S—C4S	-176.4 (6)

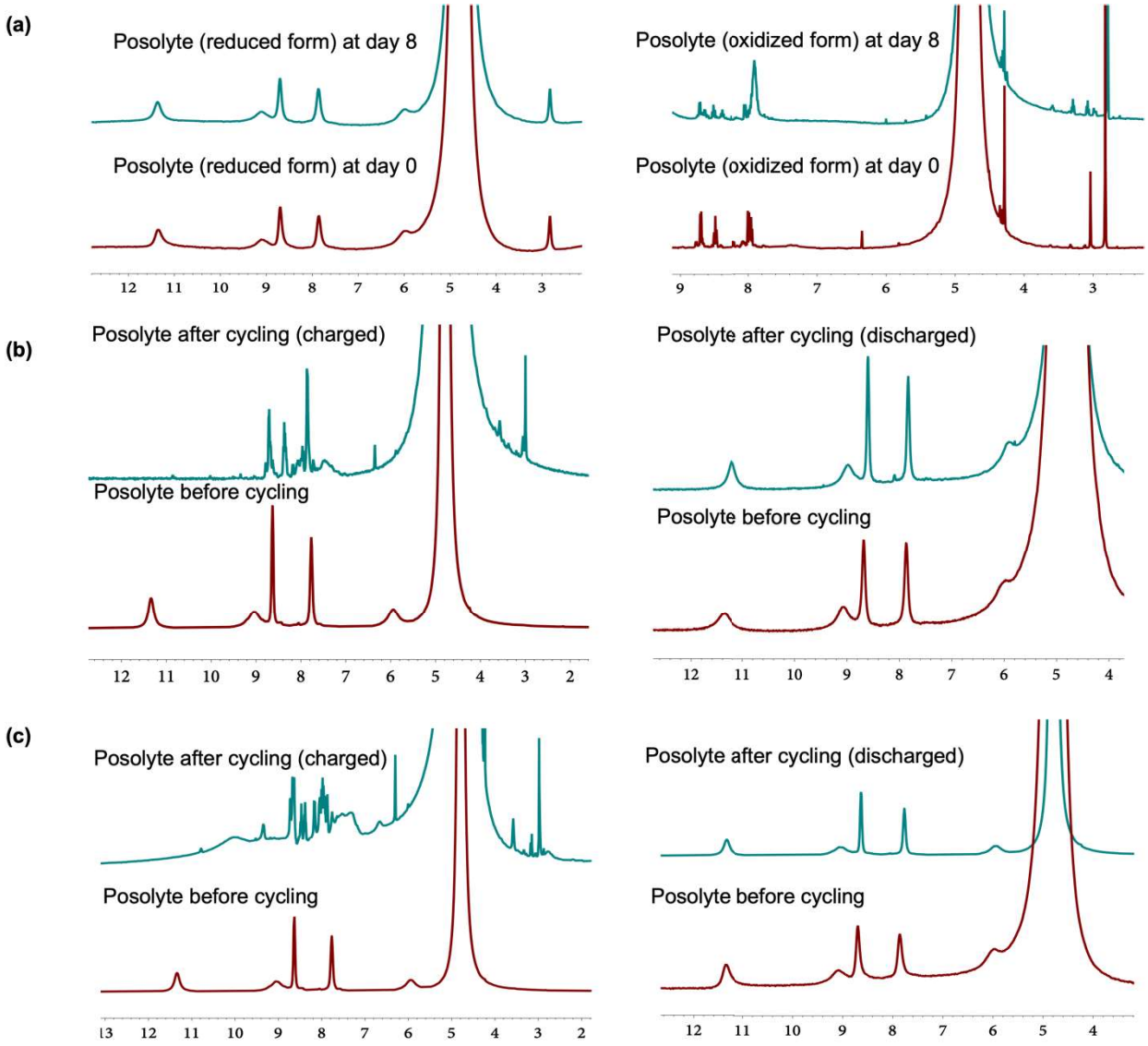


Figure S3. NMR spectra for posolyte before and after cycling. (a) Thermal stability tests for reduced and oxidized forms of 0.1 M Fe(TPEN) in 1M NaCl solution. ^{1}H-NMR spectra for reduced and oxidized forms of Fe(TPEN) incubated at 65 °C for 0 and 8 days are shown. All the ^{1}H-NMR spectra were recorded in D_2O with 10 mM sodium methanesulfonate as the internal standard. (b) ^{1}H-NMR analysis of 0.1 M posolytes before and after cell cycling, which stopped at charged and discharged state, respectively. (c) ^{1}H-NMR analysis of 0.6 M posolytes before and after cell cycling, which stopped at charged and discharged state, respectively. All the ^{1}H-NMR spectra were recorded in D_2O. No obvious new peaks were observed for posolyte stopped at discharged state before and after cycling.

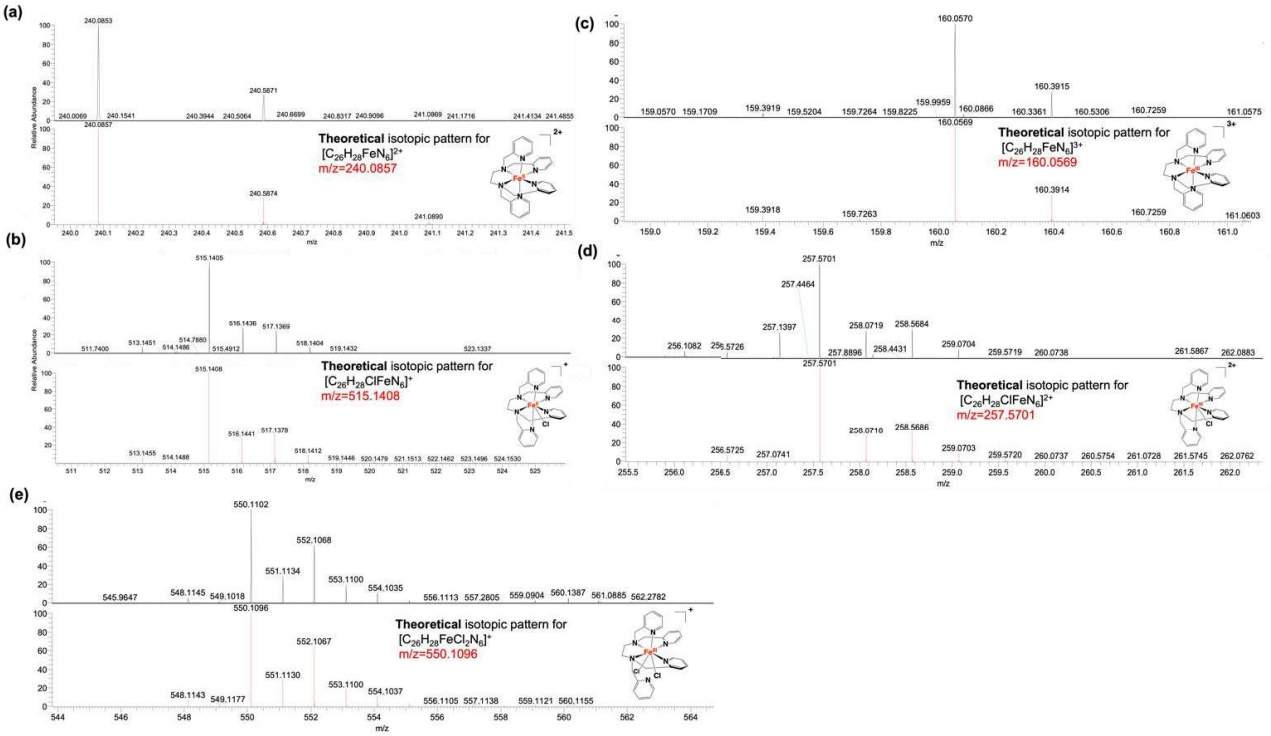


Figure S4. Raw mass spectrometry data for posolyte in BTMAP-Vi | $Fe(TPEN)Cl_2$ cell (0.6 M) after cycling, searched against target (a) $[C_{26}H_{28}ClFeN_6]^{2+}$, m/z=240.0857; (b) $[C_{26}H_{28}ClFeN_6]^{+}$, m/z=515.1408; (c) $[C_{26}H_{28}FeN_6]^{3+}$, m/z=160.0569; (d) $[C_{26}H_{28}ClFeN_6]^{2+}$, m/z=257.5701; (e) $[C_{26}H_{28}Cl_2FeN_6]^{+}$, m/z=550.1096.

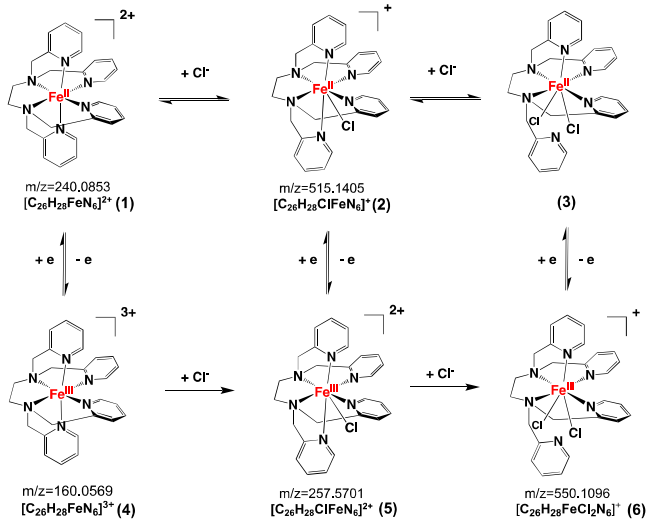


Figure S5. Proposed degradation mechanism of $Fe(TPEN)Cl_2$ (**1**) during cell cycling.

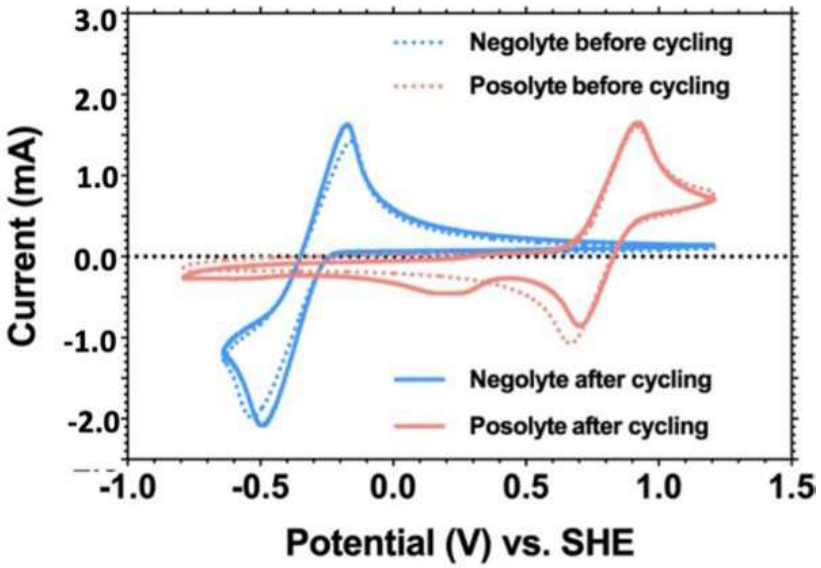


Figure S6. Cyclic voltammograms of the negolytes and posolytes before and after cycling for ARFBs using $Fe(TPEN)Cl_2$ as the posolyte species.

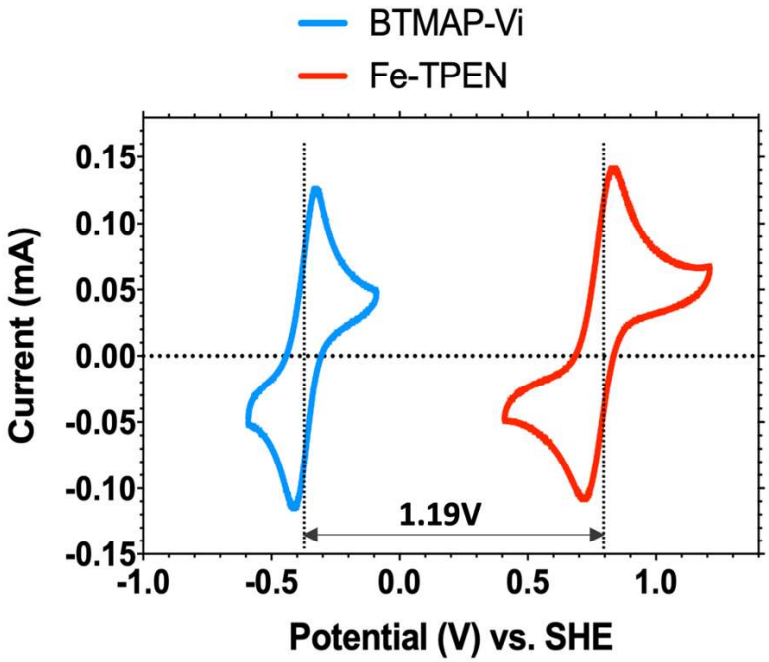


Figure S7. Cyclic voltammograms of Fe(TPEN) (red trace) and BTMAP-Vi (blue trace). The electroactive compounds were tested at 10 mM in 1 M NaCl solution at a scan rate of 100mV s^{-1}, on a glassy carbon working electrode.

Table S3. Comparison of $Fe(TPEN)Cl_2$ and other posolyte species reported previously.

Posolyte species	Redox potential (V versus SHE)	Capacity fade rate (per day)	Solubility (M)	pH	Reference
0.1 M $Na_4[Fe^{II}(Dcbpy)_2(CN)_2]$	0.86 V	0.217%	1.09	Neutral pH	[8]
1.3 M BTMAP-Fc	0.39 V	0.1%	1.9	Neutral pH	[9]
0.1 M FQH2	0.7 V	2.5%	1.4	0	[10]
1.5 M Methylene blue (MB)	0.57 V	0.76%	1.8	-0.7	[11]
0.05 M Basic blue 3 (BB3)	0.54 V	1.44%	2.5	-0.5	[12]
0.1 M Fc-HP-β-CD	0.5 V	4.08%	0.28	Neutral pH	[13]
0.1 M $Fe(CN)_6^{3-/4-}$	0.45 V	0%	0.62	Neutral pH	[14]
0.1 M $Fe(bpy)_3$	1.03 V	0.6%	0.8	Neutral pH	[15]
0.1 M $Fe(Bhmbpy)_3$	0.985 V	0.07%	0.98	Neutral pH	[16]
0.5 M FeNCl	0.61 V	0.528%	4	Neutral pH	[17]
0.6 M $Fe(TPEN)Cl_2$	0.79 V	0.28%	1.46	Neutral pH	This work

References:

[1] Bruker AXS APEX3, Bruker AXS, Madison, Wisconsin, 2015.

[2] L. Krause, R. Herbst-Irmer, G. M. Sheldrick, D. Stalke, *J. Appl. Crystallogr.* 2015 **48**, 3-10.

[3] G. M. Sheldrick, *Acta Cryst*. 2015. A**71**, 3-8.

[4] G. M. Sheldrick, *Acta Cryst*. 2015, C**71**, 3-8.

[5] O. V. Dolomanov, L. J. Bourhis, R. J. Gildea, J. A. K. Howard and H. Puschmann *J. Appl. Cryst.* 2009, 42, 339-341

[6] Accelrys DS Visualizer v2.0.1, Accelrys Software. Inc., 2007.

[7] Tang, H., Arulsamy, N., Radosz, M., Shen, Y., Tsarevsky, N.V., Braunecker, W.A., Tang, W. and Matyjaszewski, K., *J. Am. Chem. Soc.* 2006, 128, 50, 16277–16285